3D real-time and in situ characterisation of fibre kinematics in dilute non-Newtonian fibre suspensions during confined and lubricated compression flow

Tanguy Laurencin, Laurent Orgéas, Pierre J.J. Dumont, Sabine Rolland Du Roscoat, Patrice Laure, Steven Le Corre, Luisa Silva, Rajmund Mokso, Maxime Terrien

▶ **To cite this version:**

Tanguy Laurencin, Laurent Orgéas, Pierre J.J. Dumont, Sabine Rolland Du Roscoat, Patrice Laure, et al.. 3D real-time and in situ characterisation of fibre kinematics in dilute non-Newtonian fibre suspensions during confined and lubricated compression flow. Composites Science and Technology, 2016, 134, pp.258-266. ⟨10.1016/j.compscitech.2016.09.004⟩. ⟨hal-01371009⟩

HAL Id: hal-01371009

https://minesparis-psl.hal.science/hal-01371009v1

Submitted on 1 Apr 2026

HAL is a multi-disciplinary open access archive for the deposit and dissemination of scientific research documents, whether they are published or not. The documents may come from teaching and research institutions in France or abroad, or from public or private research centers.

L'archive ouverte pluridisciplinaire **HAL**, est destinée au dépôt et à la diffusion de documents scientifiques de niveau recherche, publiés ou non, émanant des établissements d'enseignement et de recherche français ou étrangers, des laboratoires publics ou privés.

Distributed under a Creative Commons CC BY 4.0 - Attribution - International License

3D real-time and *in situ* characterisation of fibre kinematics in dilute non-Newtonian fibre suspensions during confined and lubricated compression flow

T. Laurencin[a,b,c], L. Orgéas[a*], P.J.J. Dumont[b], S. Rolland du Roscoat[a], P. Laure[c], S. Le Corre[d], L. Silva[e], R. Mokso[f], M.Terrien[g]

[a]*CNRS, Univ. Grenoble Alpes, 3SR Lab, F-38000 Grenoble, France*
[b]*Univ. Lyon, LaMCoS, INSA-Lyon, CNRS UMR5259, F-69621, Lyon, France*
[c]*CNRS, Univ. Nice, Lab. J.A.Dieudonné,Parc Valrose F-06000 Nice, France*
[d]*Univ. Nantes, LTN, La Chantrerie, rue Christian Pauc - CS 50609, 44306 Nantes cedex 3, France*
[e]*Ecole Centrale de Nantes, ICI, 1 rue de la Noë F-44000 Nantes, France*
[f]*Paul Scherrer Institut, SLS, TOMCAT Beamline, 5232 Villingen, Switzerland*
[g]*CNRS, Univ. Grenoble Alpes, LGP2, F-38000 Grenoble, France*

Date : 25 July 2016

Abstract

The physical and mechanical properties of short fibre-reinforced polymer composites depend on the geometry, content, distribution and orientation of fibres within the polymer matrix. These microstructure features are mainly induced during the forming stage, *i.e.*, when composites usually flow in moulds and behave as non-Newtonian fibre suspensions. Their flow-induced microstructures still cannot be well predicted by current rheological models. To better understand them, non-Newtonian dilute fibre suspensions were prepared and subjected to lubricated compression experiments using a micro-rheometer mounted in a synchrotron X-ray microtomograph. These experiments enabled, for the first time, fast and *in situ* 3D imaging of the translation and rotation of fibres in the suspending fluid. Fibre motions were compared with the prediction of the Jeffery's model. Despite the use of a non-Newtonian suspending fluid and confined flow conditions, *i.e.*, with a gap between compression platens of the same order of magnitude than the fibre length, we showed that Jeffery's prediction was satisfactory if the fibres were sufficiently far from the compression platens (approximately at a

* Corresponding author. Tel.: +33 476 827 073; e-mail: Laurent.Orgeas@3sr-grenoble.fr .

distance of once to twice their diameter). Otherwise, the experimental average orientation rates were higher than the Jeffery's prediction.

Keywords: A. Short-fibre composites; D. Rheology; D. Microtomography; E. Injection moulding; E. Compression moulding

1. Introduction

Owing to their interesting functional and mechanical properties, and to their cost-efficient processing, short fibre-reinforced polymer composites are widely used to produce parts with fibrous microstructures (shape, aspect ratio, concentration and orientation of fibres) that are mainly induced by the forming process (film casting, extrusion, injection moulding or compression moulding) [1-5]. During these phases, the composites behave as fibre suspensions with a complex rheology which is still not very well characterised and modelled because of the difficulties to properly observe, understand and analyse evolving fibrous microstructures and flow mechanisms at the fibre scale in non-Newtonian suspending polymer matrices.

All current rheological models which describe the kinematics of fibres in polymer composites during forming are based on the pioneering and fundamental work of Jeffery [6]. However, Jeffery's model is theoretically valid for a single ellipsoidal rigid particle immersed in an infinite and incompressible Newtonian fluid flowing at low Reynolds number. For a slender ellipsoid i with an orientation given by the unit vector

$$\mathbf{p}^i = \sin\theta^i \cos\varphi^i \mathbf{e}_1 + \sin\theta^i \sin\varphi^i \, \mathbf{e}_2 + \cos\theta^i \mathbf{e}_3, \quad (1)$$

$\left(\theta^i \epsilon [0, \pi] \text{ and } \varphi^i \epsilon [0, 2\pi]\right)$, Jeffery's model describes the velocity $\mathbf{v}^i$ of its centre of mass as an affine function of the macroscale velocity gradient $\boldsymbol{\nabla}\mathbf{v}$ of the suspending

fluid. Considering the particular case of homogeneous macroscale fluid flow situations without rigid body motions, the position $\mathbf{x}^i$ of the centre of mass of the ellipsoid can thus be predicted by integrating the equation:

$$\mathbf{v}^i = \boldsymbol{\nabla}\mathbf{v} \cdot \mathbf{x}^i. \tag{2}$$

Its orientation is also given from the well-known expression for the rotation rate of $\mathbf{p}^i$:

$$\dot{\mathbf{p}}^i = \boldsymbol{\Omega} \cdot \mathbf{p}^i + \lambda\left(\mathbf{D} \cdot \mathbf{p}^i - \left(\mathbf{p}^i \cdot \mathbf{D} \cdot \mathbf{p}^i\right)\mathbf{p}^i\right), \tag{3}$$

where $\boldsymbol{\Omega} = (\boldsymbol{\nabla}\mathbf{v} - {}^t\boldsymbol{\nabla}\mathbf{v})/2$ and $\mathbf{D} = (\boldsymbol{\nabla}\mathbf{v} + {}^t\boldsymbol{\nabla}\mathbf{v})/2$ are the macroscale rotation rate and strain rate tensors, respectively, and where λ is the ellipsoid shape factor. The relevance of Jeffery's model for Newtonian fluids was confirmed experimentally by several authors [7-10], mainly in shear flow. The validity of Jeffery's equation was extended to any axisymmetric particle [11-12]. For straight cylindrical fibres of length l and diameter d, λ is a function of the fibre aspect ratio $r = l/d$:

$$\lambda = 1 - \frac{3C \ln r}{4\pi r^2}, \tag{4}$$

where $C \approx 5.45$ is a constant determined by Cox [13] from the experiments of Anczurowski and Mason [14]. Jeffery's model has largely been validated and used for dilute Newtonian fibre suspensions [10,14-16], *i.e.*, for situations where the volume fraction of fibres $\phi \ll 1/r^2$. In these situations, a compact description of the fibre orientation is often employed using the fibre orientation distribution function or its moments, *e.g.* the second $\mathbf{A}$ and fourth order $\mathbb{A}$ orientation tensors [17]. Adopting a discrete form for N fibres contained in an elementary volume of the suspension, these tensors are respectively expressed as follows:

$$\mathbf{A} = \frac{1}{N}\sum_{i=1}^{N} \mathbf{p}^i \otimes \mathbf{p}^i \qquad \mathbb{A} = \frac{1}{N}\sum_{i=1}^{N} \mathbf{p}^i \otimes \mathbf{p}^i \otimes \mathbf{p}^i \otimes \mathbf{p}^i. \tag{5}$$

In the semi-dilute regime, *i.e.*, when $1/r^2 \ll \phi \ll 1/r$, Jeffery's equations (3) are known to overestimate the fibre reorientation rate in Newtonian systems, since they do not account for long range hydrodynamic interactions between fibres [10,18-21]. In the concentrated regime, *i.e.*, when $\phi \gg 1/r$, Jeffery's equation also fails, the situation becoming more complex due to short range (non-)hydrodynamic interactions between fibres [21-24]. For these two regimes, several modifications of Eq.(3) have been proposed based on the pioneering work of Folgar and Tucker [18,25]. Departures of the fibre orientation from the Jeffery's orbits have also been observed for non-Newtonian fluids, mostly for shear flows. Hence, using viscoelastic fluids, fibres were found to align along the shear or the vorticity directions, depending on the Weissenberg number, *e.g.* by changing the shear rate or the fluid viscoelastic properties [26-28]. These experimental results were also found numerically and implemented in constitutive theories [29-32]. However, few experimental, theoretical, and numerical studies focused on fibre kinematics in shear-thinning fluids, whereas this rheological behaviour is typical for industrial polymers, as those that are used in composites. Besides, to the authors' knowledge, fibre kinematics during compressive or elongational flow are rarely analysed [16,22], whereas these flow modes are prone to occur during short fibre-reinforced polymer composite forming.

In addition, Jeffery-based theories were established for good scale separation conditions, *i.e.*, when the size of fibres is small compared with the typical size of flowing samples. Unfortunately, this critical prerequisite is rarely fulfilled by the composite forming conditions. In many situations, composites flow through narrow channels or in thin mould cavities with gaps h being in the same order of magnitude as the fibre length l. These flow situations correspond to confined regimes [33-35]: the

scale separation between the sample and its heterogeneities is poor so that fibres are close to the mould walls. It is well-known that when fibres interact with a solid wall, departures from the Jeffery's trajectories and orbits are prone to occur [36-38]. Few theoretical studies proposed modifications of Jeffery's equations to account for confinements and/or wall effects [33,39-41]. To the best of the authors' knowledge, these effects have rarely been studied for non-Newtonian suspending fluids [36], and never been analysed for elongational or compression flows.

Lastly, it is also interesting to mention that in most of the aforementioned experimental studies, fibre kinematics was followed using 2D optical approaches [7-10,14,18-19,26-28,36-38,42], 2D wide-angle X-ray diffraction [43], or high speed X-ray phase-contrast 2D imaging [16]. These techniques work for dilute suspensions but have limitations for semi-dilute and concentrated fibre suspensions. In addition, they do not offer 3D views of fibres and their kinematics. In parallel, X-ray micro-tomography has become a powerful technique to provide 3D images of fibrous architectures [23,44-45]. Using appropriate image analysis procedures, relevant microstructure descriptors such as the position, orientation of fibres and fibre-fibre contacts can be extracted [5,46-49]. Thanks to *in situ* rheometry, it is also possible to follow the evolution of these descriptors during rheological tests [46,48]. However, these analyses are restricted to interrupted mechanical loadings, due to the usually long scanning times that are required with standard X-ray sources. Recent synchrotron X-ray sources have made possible to acquire 3D images at very fast scanning times, and thus to perform real-time 3D *in situ* observations during the deformation of imaged samples [50].

Hence, the main objective of this contribution was to experimentally investigate the relevance of Jeffery's theory for modelling fibre kinematics in fibre suspensions with

shear-thinning suspending fluids when they are subjected to confined and lubricated compression flow. For that purpose, model dilute and non-Newtonian fibre suspensions were prepared and compression experiments were performed using a specially designed micro-rheometer mounted on the rotation stage of a synchrotron X-ray microtomograph. Combined with dedicated image analysis procedures, these experiments enabled, for the first time, fast and real-time 3D observations of the translation and rotation of fibres to be obtained and compared with the prediction of Jeffery's model.

2. Materials and experimental procedure

2.1. Materials

A hydrocarbon gel (paraffin) was used as suspending fluid for the studied fibre suspensions [47]. Its transparency facilitated the control of the fibre microstructure during the suspension preparation. The hydrocarbon gel viscosity was tunable with the temperature. At 120°C, this polymer behaved as a Newtonian fluid and its shear viscosity was approximately 1 Pa s. At room temperature, it behaved as a solid gel (Fig. 1(c)), so that the suspensions could be easily handled before the experiments, without damaging their microstructures. Finally, at 50°C, the hydrocarbon gel exhibited a non-Newtonian behaviour close to that of industrial polymer matrices used in composites. Fig. 1(a) shows that its shear viscosity μ is a shear-thinning power-law, *i.e.*, $\mu = K\dot{\gamma}^{n-1}$ where $\dot{\gamma} = \sqrt{2\mathbf{D}:\mathbf{D}}$ is the generalised shear rate, and where the power-law exponent $n = 0.2$ and the consistency $K = 440$ Pa s$^{1\text{-}n}$ were determined using a cone-plane rheometer (Anton Paar MCR301). The fibres used in the suspensions were cut from a PVDF fishing wire (diameter $d = 200\,\mu$m, Young's modulus ≈ 2 GPa), exhibiting a sufficiently different X-ray absorption coefficient when compared with the hydrocarbon gel [46].

Test number	1	2	3	4	5	6	7	8	9
N	1	1	1	1	1	1	5	8	8
ϕ (%)	0.013	0.013	0.015	0.013	0.011	0.011	0.11	0.21	0.16
r	16.5	17	19.5	17.5	14.5	14.5	12.6	17.9	17.7
D_{33}^0 (s^{-1})	0.004	0.004	0.03	0.03	0.03	0.03	0.03	0.004	0.03
Δx_{min}^i(%)	-	-	-	-	-	-	2.0	2.1	1.5
Δx_{max}^i(%)	8	7.5	8.2	5.6	7.6	7.2	4.1	7.1	5.9

Table 1. Test number and conditions: number of fibres N and fibre aspect ratio r in the investigated suspensions, initial strain rate D_{33}^0 used for the compression test, minimal Δx_{min}^i and maximal Δx_{max}^i recorded deviations for the position of the fibre centres of mass of fibres with respect to the affine assumption.

To prepare the fibre suspensions, fibres were cut at a constant length l from continuous wire with a razor blade at targeted aspect ratios $r = l/d$ (Tab. 1) to avoid blunt-ended extremities (Fig. 1(b)). The suspensions were hand-made layer by layer while keeping the control of the fibre orientation. The process consisted in picking fibres with desired orientations in a thin layer of the solid gel and impregnating these fibres with a second layer of pre-heated gel at 120°C. Suspensions were fabricated in cylindrical moulds (diameter $D_0 = 14$ mm, height $h_0 = 5$ mm). Following this preparation method, nine samples were fabricated. For six samples, one fibre was placed in their centre with different initial orientations (θ^i, φ^i). Three samples had five to eight fibres (Fig. 1(c)), corresponding to a dilute concentration regime ($\phi \ll 1/r^2$), as summarized in Tab. 1.

2.2. Compression experiments with real-time 3D in situ X-ray imaging

The fibre model suspensions were subjected to lubricated compression loading using a specially designed compression micro-rheometer (Fig. 1(d)). To perform the experiments at 50°C, heaters and thermocouples were inserted inside the compression platens. Before compression, the platens were lubricated with silicone oil, and the suspensions were subjected to a small pre-compression to ensure the contact with them.

After stress relaxation and temperature homogenization ($\approx 10\,\mathrm{min}$), the mechanical loading was applied through a piezoelectric actuator attached to the lower compression platen. The compression tests were performed at two constant actuator velocities $\dot{h}$, corresponding to two initial strain rates $D_{33}^0 = \dot{h}/h_0$ along the $\mathbf{e}_3$-direction (Tab. 1). A displacement sensor (Fig. 1(d)) enabled the height of the suspension h and the compression strain $\varepsilon_{33} = \ln(h/h_0)$ to be precisely measured. It is important to notice that the rheology of the suspending fluid was non-linear and highly shear-thinning for the studied strain rates, as shown in Fig. 1(a), and that the studied confined flow situations were close to those encountered during forming of short-fibre reinforced composites , *i.e.*, with a poor scale separation such that $l/h = \mathcal{O}(1)$ [33-35].

To characterise the 3D suspension fibrous microstructures during compression, the rheometer was placed inside a synchrotron X-ray microtomograph (TOMCAT beamline, Swiss Light Source, Paul Scherrer Institut, Villingen, Switzerland). Ten scans were taken during each compression test, *i.e.*, without interrupting the compression experiment, using the following acquisition parameters for each 3D image: 601 X-ray projections (20 KeV, 400 mA) were acquired over a 180° rotation of the micro-rheometer for a short scanning time of 0.42 s. Using the Paganin reconstruction mode and suitable reconstruction algorithms, 3D images of scanned specimen were obtained with a size of $1776 \times 1776 \times 450$ voxel and a voxel size of $11 \times 11 \times 11\ \mu\mathrm{m}^3$.

2.3. Image analysis and data post-treatment

By using standard filtering and thresholding operations (implemented into the software Fiji [51]), 3D binarised images of the matrix and the fibrous microstructures of the suspensions were built (Fig. 2). Then:

- To verify both the homogeneity and the incompressibility of the suspension flow, the free surface of samples was detected and followed during compression thanks to the function "Outline" implemented in Fiji, as shown in Fig. 3(a-c). This function was used for each horizontal slice in the 3D images, except for two sets of 10 slices located near the compression platens where it was difficult to distinguish the suspensions because of the metallic nature of the platens. This enabled the sample mean surface $\bar{S}$ perpendicular to the compression axis $\mathbf{e}_3$ to be determined, as well as the macroscale sample Hencky surface strain $\varepsilon_S = \ln(\bar{S}/\bar{S}_0)$.
- Other image analysis operations were performed using the softwares Fiji, Avizo and Matlab to analyse quantitatively the evolution of the fibrous microstructure of the investigated suspensions, following the methodology reported by Latil *et al.* [46]. After segmentation, the fibre centrelines were extracted using a skeletonisation algorithm implemented in Avizo and then smoothed. This enabled the fibre orientation (tangent) vector $\mathbf{p}^i$, the second and fourth order orientation tensors $\mathbf{A}$ and $\mathbb{A}$, and the position of the centre of mass $\mathbf{x}^i$ of each fibre i to be calculated for each 3D image of each experiment (Fig. 3(a-b)). Finally, thanks to the low concentration in fibres, it was easy to follow the trajectory of each fibre during compression experiments using a fibre centreline tracking algorithm based on a discrete correlation distance function [52].
- The relevance of Jeffery's model was assessed, *i.e.*, we verified the validity of the affine assumption Eq. (2) and the orientation equation Eq. (3) for the prediction of the position of the centre of mass $\mathbf{x}^i_{Jeff}$ and the orientation vector $\mathbf{p}^i_{Jeff}$ of each fibre i. We also estimated the second order fibre orientation tensor $\mathbf{A}_{Jeff}$ directly from Eq. (5) and the orientation vectors $\mathbf{p}^i_{Jeff}$. For that purpose, Eqs. (2-3) were numerically integrated using the fourth order Runge-Kutta scheme implemented in Matlab, assuming that the

macroscale suspension flow was homogeneous (point 1 in section 3), incompressible ($\boldsymbol{\nabla} \cdot \mathbf{v} = 0$, point 1 in section 3) and irrotational ($\boldsymbol{\Omega} = \mathbf{0}$). Further, the strain rate tensor $\mathbf{D}$ was estimated from the height of the suspension h measured using the 3D images with a maximum error of ± 1 voxel. As initial conditions, the positions $\mathbf{x}_0^i$, the orientation vectors $\mathbf{p}_0^i$ (and the tensor $\mathbf{A}_0$) were obtained from the images corresponding to the initial undeformed configurations, with maximum errors of ± 1 voxel and $\pm 0.15°$, respectively. Then, two thousand integrations per experiment were computed using errors associated with h, $\mathbf{x}_0^i$, and $\mathbf{p}_0^i$ that were randomly chosen within the aforementioned ranges. This enabled the errors on the corresponding integrated parameters to be estimated. Here, the errors were considered to correspond to the difference between the 2nd and 98th percentile values of the computed distributions.

3. Results and discussion

Experimental results are shown in Figs. 3-7. Fig. 3 allows us to characterise the flow homogeneity and the incompressibility of samples during compression. Figs. 3(a-c) show 3D and 2D views of the free surface of one typical sample during compression, whereas Fig. 3(d) shows the evolution of the sample surface strain ε_S as a function of the compression strain $|\varepsilon_{33}|$. Figs. 4(a-b) show the paths $\mathbf{x}^i$ followed by each fibre centre of mass during suspension flow, for sample 1 with only one fibre (Tab.1) and for sample 9 with eight fibres (Tab. 1), respectively. For comparison purposes, these figures also show the paths $\mathbf{x}_{Jeff}^i$ predicted by Jeffery'model (Eq.(2)). In addition, Figs. 4(c-d) show the evolution of the deviation $\Delta x^i = \left\|\mathbf{x}^i - \mathbf{x}_{Jeff}^i\right\|/h_0$ of the experimental position of the fibre centre of mass $\mathbf{x}^i$ with respect to $\mathbf{x}_{Jeff}^i$, for samples 1 to 6 (containing only one fibre) and for sample 9, respectively. The minimal Δx_{min}^i and

maximal Δx_{max}^{i} values of this deviation are also given in Tab. 1 for all tested samples. The two graphs in Fig. 5 show the evolution of the orientation angles θ^i and φ^i as a function of the compression strain $|\varepsilon_{33}|$ for samples 1 to 6. For comparison purposes, the angles predicted by Jeffery's model (Eqs.(3-4)) are also plotted in this figure. Fig. 6 is similar to Fig. 5 but shows data for samples 7 to 9, *i.e.*, samples containing five to eight fibres (Tab.1). Lastly, Fig. 7 gives the evolution with $|\varepsilon_{33}|$ of the experimental and predicted diagonal components a_{ii} of the second order fibre orientation tensor **A** during the compression of samples 7 to 9. From these figures, some comments can be made:

1. The 3D views in Fig. 3(a-b) and the vertical profiles of the evolving free surface in the $(\mathbf{e}_2, \mathbf{e}_3)$ plane (Fig.3(c)), which nearly kept their initial dimensionless shape during flow prove that due to the lubrication of the compression platens, the flow of samples was practically homogeneous and exhibited compressive plug flow velocity profiles [53] with negligible transverse shear stresses. Thus, as a first approximation, the macroscale stress states during the experiments were considered to be homogeneous simple compression stress states. In addition, Fig. 3(d) shows that the macroscale Hencky surface strain ε_S was close to the absolute value of the macroscale Hencky compression strain $|\varepsilon_{33}| = -\varepsilon_{33}$. Consequently, the compression flow of the suspensions was considered to be incompressible since $\mathrm{tr}(\boldsymbol{\varepsilon}) = \varepsilon_S + \varepsilon_{33} \approx 0$ ($\boldsymbol{\varepsilon}$ being the Hencky strain tensor). Lastly, we also verified that the flow of samples in the perpendicular directions to the compression axis was isotropic. Therefore, these observations show (i) that a proper estimate of the macroscale strain rate tensor **D** for these experiments was:

$$\mathbf{D} = \frac{\dot{h}}{h}\left(\mathbf{e}_3 \otimes \mathbf{e}_3 - \frac{1}{2}\,\mathbf{e}_1 \otimes \mathbf{e}_1 - \frac{1}{2}\mathbf{e}_2 \otimes \mathbf{e}_2\right), \tag{6}$$

and (ii) that, in the dilute concentration regime, fibre scale flow perturbations induced by the presence of fibres did not induce noticeable macroscale flow modifications, whereas the opposite trend was obtained for concentrated fibre suspensions in similar compression conditions [22].

2. Figs. 4(a-b) show that the fibres were transported with the non-Newtonian suspending fluid during compression experiments: the positions of their centre of mass went towards the upper compression platen and progressively moved parallel to the $(\mathbf{e}_1, \mathbf{e}_2)$ plane. As evident from these graphs, these motions were almost affine functions of the macroscale suspending fluid kinematics as the experimental trajectories and their predictions using Eq. (2) with adequate initial and boundary conditions nearly coincided. Besides, as shown quantitatively in Fig. 4(c-d) and given in Tab. 1, the deviations Δx^i of the experimental data from the affine assumption increased with the compression strain $|\varepsilon_{33}|$, but never exceeded 9%, regardless of the sample. It was difficult to determine whether these deviations had physical origins such as, for example, small shear flow mechanisms related to non-ideal lubrication conditions between the samples and the compression platens, or were induced by experimental artefacts such as, for example, unexpected rigid body motions of compressed samples. Anyway, for the investigated experimental conditions, these deviations were limited and it was fair to conclude that the translations of fibres followed, at least at first order, the affine assumption in Eq. (2) of Jeffery's model. For suspensions with several fibres (samples 7 to 9), this tends to prove that the (long range) hydrodynamic interactions between the fibres themselves

or between the fibres and the compression platens had rather weak consequences on the fibre translations.

3. Fig. 5 reveals that during compression of the samples with one centred fibres, fibres progressively aligned along the $(\mathbf{e}_1, \mathbf{e}_2)$ plane, regardless of their initial orientation and aspect ratio, and the initial macroscale strain rate. The out-of-plane angles θ^i gradually increased with increasing the compression strain $|\varepsilon_{33}|$, the increasing rate being higher when the initial angles θ_0^i were far from 90°. In parallel, it is interesting to note that the in-plane angles φ^i practically remained unaffected during the same compression experiments. In addition, it is also worth noting that the experimental values of the angles θ^i and φ^i were very close to those predicted by Jeffery's model (Eqs. (4-5)). Indeed, the maximum deviations of the angles θ^i and φ^i from the model predictions remained below 1 and 2°, respectively. Combined with results discussed in the previous point, these results validate, at first order, the use of Jeffery's theory for the prediction of the motion of single, centred, straight and cylindrical fibres within a shear-thinning fluid compressed in a narrow gap with $l/h = \mathcal{O}(1)$.
4. Regardless of the investigated fibre aspect ratio and strain rate, the orientation results obtained for dilute suspensions with several fibres were qualitatively similar, as illustrated in Fig. 6. The angles θ^i increased with increasing $|\varepsilon_{33}|$ and the angles φ^i remained more or less constant, except for some fibres for which the angle φ^i slightly varied with $|\varepsilon_{33}|$ (these fibres are indicated by the arrows in Fig. 6). However, this figure clearly shows that Jeffery's predictions were less relevant than those obtained for single centred fibres (Fig. 5). The same trend is observed in Fig. 7 for the evolution of the diagonal components a_{ii} of $\mathbf{A}$ (note that the non-diagonal components that were very small were omitted in the graph for clarity). This figure

shows that Jeffery's predictions underestimated the overall fibre orientation rate. They were still satisfying for samples 7 and 8, and rather far from experiments for sample 9. Accounting for the results discussed in point 3, the origins of these deviations could rather be related to hydrodynamic interactions of the considered fibres (i) with their neighbours and/or (ii) with the compression platens, *i.e.*, the so-called confinement effects, than to the shear-thinning and non-Newtonian behaviour of the suspending fluid. The first type of hydrodynamic interactions is expected to be weak since the studied suspensions belonged to the dilute regime (Tab. 1). The 3D images enabled us to evidence that the second type of interactions occurred. This was done by detecting fibres that were in the vicinity of the compression platens, *i.e.*, when the distance of the fibres from the platens was once to twice the fibre diameter d, which corresponds to a typical distance below which short range hydrodynamic interactions could occur. These fibres and the evolution of their corresponding angles are shown in Figs. 2 and 6 with orange arrows. As an example, the evolution of the angle θ^i of the fibre represented with pink circles in Fig. 6(e) exhibited a departure from its initial Jeffery-like trajectory for $\varepsilon_{33} > 0.3$. This phenomenon occurred when this fibre was very close to the two compression platens (see the two arrows that points to this fibre in Fig. 2), thus inducing a departure of the fibre orientation from a Jeffery-like orbit. As shown in Fig. 6, the highest deviations from the Jeffery's predictions for the angles θ^i were higher for sample 9 that had several fibres close to the compression platens than for sample 8, whereas there was no fibre close to the platens in sample 7.

5. It is interesting to note that within the investigated strain rate range, the kinematics of fibres was nearly independent of the macroscale compression strain rate. Indeed,

when fibres were sufficiently far from the wall, changing the compression strain rate by a factor of ten did not drastically alter the trajectory of the centre of mass of the fibres, nor their orientation evolution which practically followed the Jeffery's orbits (see Figs. 4 to 7). These trends differ from those observed or simulated for fibres immerged in sheared viscoelastic fluids [26-27,31].

4. Conclusion

We performed rheometry experiments on model dilute fibre suspensions with a non-Newtonian suspending fluid, by using lubricated compression experiments coupled with unprecedented real-time 3D *in situ* observations of the fibrous microstructures. This was made possible using a micro-rheometer mounted in a synchrotron X-ray microtomograph enabling both very short scanning times, *i.e.*, less than 0.5 s, and a high spatial resolution. This method was particularly efficient to analyse the fibre kinematics of each individual fibre in these model systems, the microstructures, the rheology, and the confined flow conditions of which were close to those encountered in short-fibre reinforced polymer composites during the forming stages. Regardless of the investigated conditions, *i.e.*, various fibre aspect ratios and initial orientations, we found that Jeffery's theory and its related affine assumption led to rather good estimates of the kinematics of one fibre centred in a non-Newtonian shear-thinning fluid compressed in a confined region. These results were not affected by changing the macroscale compression strain rate. Thus, at least for the investigated experimental conditions, it is fair to conclude that shear-thinning and confinement effects had minor effects on the kinematics of single fibres, provided that the distance between fibres and the walls remained sufficiently large (approximately above once to twice the fibre diameter). When the last condition was fulfilled, these results were still relevant for dilute

suspensions with several fibres, even though the motions of these fibres could be slightly altered by weak long range hydrodynamic interactions between fibres. Otherwise, more important deviations in the theoretical predictions occurred due to short range interactions of some fibres with the walls. These results must be confirmed by performing for instance fibre scale fluid flow simulations using dedicated CFD softwares [54]. They must also be completed for higher fibre concentration regimes to build relevant constitutive theories. Confinement effects such as those that have been revealed in this study are rarely taken into account in constitutive rheological theories [33,39-40], although they often occur in industrial processing conditions.

Acknowledgements – T. Laurencin gratefully acknowledges the LabEx Tec21 (Inv. d'Avenir - grant agreement n°ANR-11-LABX-0030) for his PhD research grant. We acknowledge the Paul Scherrer Institut, Villigen, Switzerland for provision of synchrotron radiation beamtime at the beamline TOMCAT of the Swiss Light Source.

References

[1] S. Advani, Flow and Rheology in Polymer Composites Manufacturing, Vol. 10 of Composite Materials Series, Elsevier, 1994.

[2] J. L. Thomasson, M. A. Vlug, Influence of fibre length and concentration on the properties of glass fibre-reinforced polypropylene: 1. tensile and flexural modulus, Compos. Part. A 27A (1996) 477–484.

[3] S. Fu, Y. Mai, Thermal conductivity of mislaligned short-fiber reinforced polymer composites, J. Appl. Polym. Sci. 88 (2003) 1497–1505.

[4] F. Danès, B. Garnier, T. Dupuis, P. Lerendu, T.-P. Nguyen, Non-uniformity of the filler concentration and of the transverse thermal and electrical conductivities of filled polymer plates, Compos. Sci. Technol. 65 (2005) 945–951.

[5] L. Orgéas, P. Dumont, J.-P. Vassal, O. Guiraud, V. Michaud, D. Favier, In-plane conduction of polymer composites plates reinforced with architectured networks of copper fibres, J. Mater. Sci. 47 (2012) 2932–2942.

[6] G. B. Jeffery, The motion of ellipsoidal particles immersed in a viscous fluid, Proc. Roy. Soc. London (A) 102 (1922) 161–179.

[7] G. Taylor, The motion of ellipsoidal particles in a viscous fluid, proceedings of the royal society of london. series a, Proc. R. Soc. London A103 (1923) 58–61.

[8] A. Binder, The motion of cylindrical particles in viscous flow, J. Appl. Phys. 10 (1939) 711.

[9] B. J. Trevelyan, S. G. Mason, Particle motions in sheared suspensions I. rotations, J. Colloid Sci. 6 (1951) 354–367.

[10] M. P. Petrich, D. L. Koch, C. Cohen, An experimental determination of the stress-microstructure relationship in semi-concentrated fiber suspensions, J. Non-Newtonian Fluid Mech. 95 (2000) 101–133.

[11] F. P. Bretherton, The motion of rigid particles in a shear flow at low reynolds number, J. Fluid Mech. 14 (1962) 284–304.

[12] H. Brenner, Rheology of a dilute suspension of axisymmetric brownian particles, Int. J. Multiphase Flow 1 (1974) 195–341.

[13] R. G. Cox, The motion of long slender bodies in a viscous fluid. II : Shear flow, J. Fluid Mech. 45 (1971) 625.

[14] E. Anczurowski, S. G. Mason, Particle motions in sheared suspensions XXIV. rotation of rigid spheroids ans cylinders, Trans. Soc. Rheol. 12 (1968) 209.

[15] M. Rahnama, D. L. Koch, E. S. G. Shaqfeh, The effect of hydrodynamic interactions on the orientation distribution in a fiber suspension subject to simple shear flow, Phys. Fluids 7 (1995) 487–506.

[16] S. Sinha-Ray, K. Fezzaa, A. L. Yarin, The internal structure of suspensions in uniaxial elongation, J. Appl. Physics 113.

[17] S. G. Advani, C. L. Tucker, The use of tensors to describe and predict fiber orientation in short fiber composites, J. Rheol. 3 (1987) 751–784.

[18] F. Folgar, C. L. Tucker, Orientation behavior of fibers in concentrated suspensions, J. Reinf. Plast. Compos. 3 (1984) 98–118.

[19] C. A. Stover, D. L. Koch, C. Cohen, Observations of fiber orientation in simple shear-flow of semidilute suspensions, J. Fluid Mech. 238 (1992) 277–296.

[20] M. Rahnama, D. L. Koch, C. Cohen, Observations of fiber orientation in suspensions subjected to planar extensional flows, Phys. Fluids 7 (8) (1995) 1811–1817.

[21] R. S. Bay, Fiber orientation in injection molded composites : A comparison of theory end experiments, Ph.D. thesis, University of Illinois, USA (1991).

[22] P. Dumont, J.-P. Vassal, L. Orgéas, V. Michaud, D. Favier, J.-E. Månson, Processing, characterization and rheology of transparent concentrated fibre bundle suspensions, Rheol. Acta 46 (2007) 639–651.

[23] T. H. Le, P. J. J. Dumont, L. Orgéas, D. Favier, L. Salvo, E. Boller, X-ray phase contrast microtomography for the analysis of the fibrous microstructure of SMC composites, Compos. Part A 39 (2008) 91–103.

[24] P. J. J. Dumont, S. Le Corre, L. Orgéas, D. Favier, A numerical analysis of the evolution of bundle orientation in concentrated fibre-bundle suspensions, J. Non-Newtonian Fluid Mech. 160 (2009) 76–92.

[25] J. Phelps, C. Tucker, An anisotropic rotary diffusion model for fiber orientation in short- and long-fiber thermoplastics, J. Non-Newtonian Fluid Mech. 156 (2009) 165–176.

[26] Y. Iso, D. L. Koch, C. Cohen, Orientation in simple shear flow of semi-dilute fiber suspensions. 1. weakly elastic fluids, J. Non-Newtonian Fluid Mech. 62 (1996) 115–134.

[27] Y. Iso, C. Cohen, D. L. Koch, Orientation in simple shear flow of semi-dilute fiber suspensions. 2. highly elastic fluids, J. Non-Newtonian Fluid Mech. 62 (1996) 135–153.

[28] D. Z. Gunes, R. Scirocco, J. Mewis, J. Vermant, Flow-induced orientation of non-spherical particles: effect of aspect ratio and medium rheology, J. Non-Newtonian Fluid Mech. 155 (2008) 39–50.

[29] L. Leal, The slow motion of slender rod-like particles in a second-order fluid, J. Fluid Mech. 69 (1975) 305–337.

[30] P. Brunn, The slow motion of a rigid particle in a second-order fluid, J. Fluid Mech. 82 (1977) 529–547.

[31] G. D'Avino, M. Hulsen, F. Greco, P. Maffettone, Bistability and metabistability scenario in the dynamics of an ellipsoidal particle in a sheared viscoelastic fluid, Phys. Rev. E 89 (2014) 043006.

[32] D. Borzacchiello, E. Abisset-Chavanne, F. Chinesta, R. Keunings, Orientation kinematics of short fibres in a second-order viscoelastic fluid, Rheol. Acta DOI 10.1007/s00397-016-0929-4.

[33] R. Schiek, E. Shaqfeh, Oscillatory shear of a confined fiber suspension, J. Rheol. 41 (1997) 445–466.

[34] B. Snook, E. Guazzelli, J. Butler, Vorticity alignment of rigid fibers in an oscillatory shear flow: Role of confinement, Phys. Fluids 24 (2012) 121702.

[35] H. Diamant, Hydrodynamic interaction in confined geometries, J Phys. Soc. Japan 78 (2009) 041002.

[36] C. A. Stover, C. Cohen, The motion of rod-like particles in pressure-driven flow between two flate plates, Rheol. Acta 29 (1990) 192–203.

[37] K. Moses, S. Advani, A. Reinhardt, Investigation of the fiber motion of fiber motion near solid boundaries in simple shear flow, Rheol. Acta 40 (2001) 296–306.

[38] A. Carlsson, F. Lundell, L. Soderberg, Fiber orientation control related to papermaking, J. Fluid Eng. – Trans. of the ASME 129 (2006) 457–465.

[39] A. Ozolins, U. Strautins, Simple models for wall effect in fiber suspension flows, Math. Model. Analysis 19 (2014) 75–84.

[40] M. Perez, A. Scheuer, E. Abisset-Chavanne, F. Chinesta, R. Keunings, A multi-scale description of orientation in simple shear flows of confined rod suspensions, J. Non-Newtonian Fluid Mech. doi:10.1016/j.jnnfm.2016.01.011.

[41] S. Bounouna, P. Kuzhir, E. Lemaire, Normal stress differences in non-brownian fiber suspensions, J. Rheol. 60 (2016) 661–671.

[42] K. Yasuda, N. Mori, K. Nakamura, A new visualization technique for short fibers in a slit flow of fiber suspensions, Int J Eng Sc 40 (2002) 1037–1052.

[43] H. Menendez, J. White, A wide-angle x-ray diffraction method of determining chopped fiber orientation in composites with application to extrusion through dies, Polymer Eng. Sci. 24 (1984) 1051–1055.

[44] M. Faessel, C. Delisée, F. Bos, P. Castera, 3d modelling of random cellulosic fibrous networks based on x-ray tomography and image analysis, Compos. Sci. Technol. 12 (2005) 1931–1940.

[45] J.-P. Suuronen, A. Kallonen, M. Elk, J. Puttonen, R. Serima, H. Herrmann, Analysis of short fibres orientation in steel fibre-reinforced concrete (sfrc) by x-ray tomograph, J. Mater. Sci. 48 (2013) 1358–1367.

[46] P. Latil, L. Orgéas, C. Geindreau, P. J. J. Dumont, S. Rolland du Roscoat, Towards the 3d in situ characterisation of deformation micro-mechanisms within a compressed bundle of fibres, Compos. Sci. Technol. 71 (2011) 480–488.

[47] O. Guiraud, L. Orgéas, P. J. J. Dumont, S. Rolland du Roscoat, Microstructure and deformation micro-mechanisms of concentrated fibre bundle suspensions: an analysis combining x-ray microtomography and pull-out tests, J. Rheol. 56 (2012) 593–623.

[48] S. Wegner, T. Borzsonyi, T. Bien, G. Rose, R. Stannarius, Alignment and dynamics of elongated cylinders under shear, Soft Matter 8 (2012) 10950–10958.

[49] J. Viguié, P. Latil, L. Orgéas, P. J. J. Dumont, S. Rolland du Roscoat, J.-F. Bloch, C. Marulier, O. Guiraud, Finding fibres and their contacts within 3d images of disordered fibrous media, Compos. Sci. Technol. 89 (2013) 202–210.

[50] N. Limodin, L. Salvo, E. Boller, M. Suery, M. Felberbaum, S. Gailliegue, K. Madi, In situ and real-time 3-d microtomography investigation of dendritic solidification in an al–10 wt.% cu alloy, Acta Mater. 57 (2009) 2300–2310.

[51] J. Schindelin, I. Arganda-Carreras, E. Frise, V. Kaynig, M. Longair, T. Pietzsch, S. Preibisch, C. Rueden, S. Saalfeld, B. Schmid, J.-Y. Tinevez, D. White, V. Hartenstein, K. Eliceiri, P. Tomancak, A. Cardona, Fiji: an open-source platform for biological-image analysis, Nature Methods 9 (2012) 676–682.

[52] S. Le Corre, P. Latil, L. Orgéas, P. Dumont, S. Rolland du Roscoat, C. Geindreau, A 3d image analysis for fibrous microstructures: discretization and fiber tracking., in: Proc of 15th Euro. Conf. Compos. Mater. (ECCM 15), Venice, Italy, 2012, pp. 1–6.

[53] M. R. Barone, D. A. Caulk, A model for the flow of a chopped fiber reinforced polymer compound in compression molding, J. Appl. Mech. 53 (191) (1986) 361–370.

[54] P. Laure, G. Beaume, O. Basset, L. Silva, T. Coupez, Numerical methods for solid particles in particulate flow simulations, Euro. J. Comput. Mech. 16 (2007) 365–383.

FIGURES

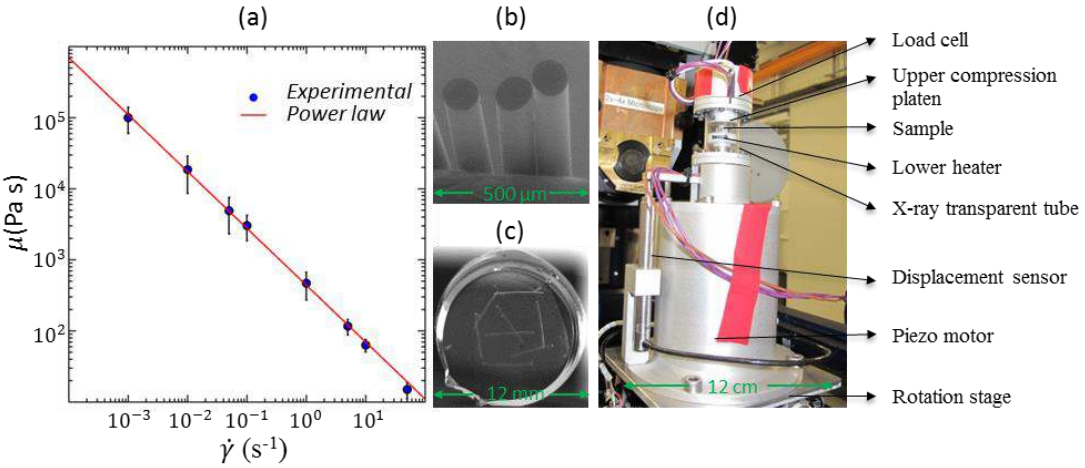

Figure 1. (a) Evolution of the shear viscosity of the hydrocarbon gel as a function of the shear rate at the testing temperature. (b) SEM micrograph showing the cut extremities of PVDF fibres. (c) Upper view of a fibre suspension sample with eight fibres. (d) Global view of the compression micro-rheometer.

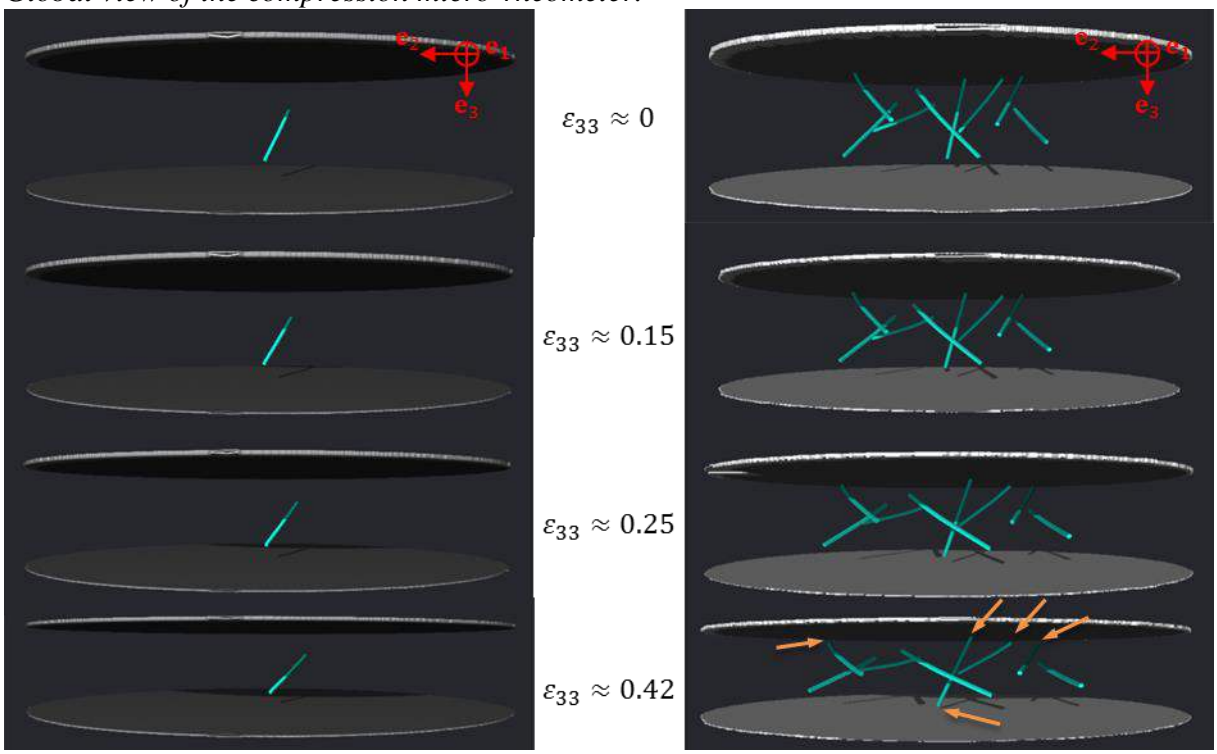

Fig. 2. 3D segmented images obtained at various compression strains ε_{33} showing the motion of the fibres of samples 1 (left) and 9 (right) during compression. The orange arrows point to the extremity of fibres that are very close to the compression platens. The orbits of these fibres deviate from the predictions of Jeffery's model.

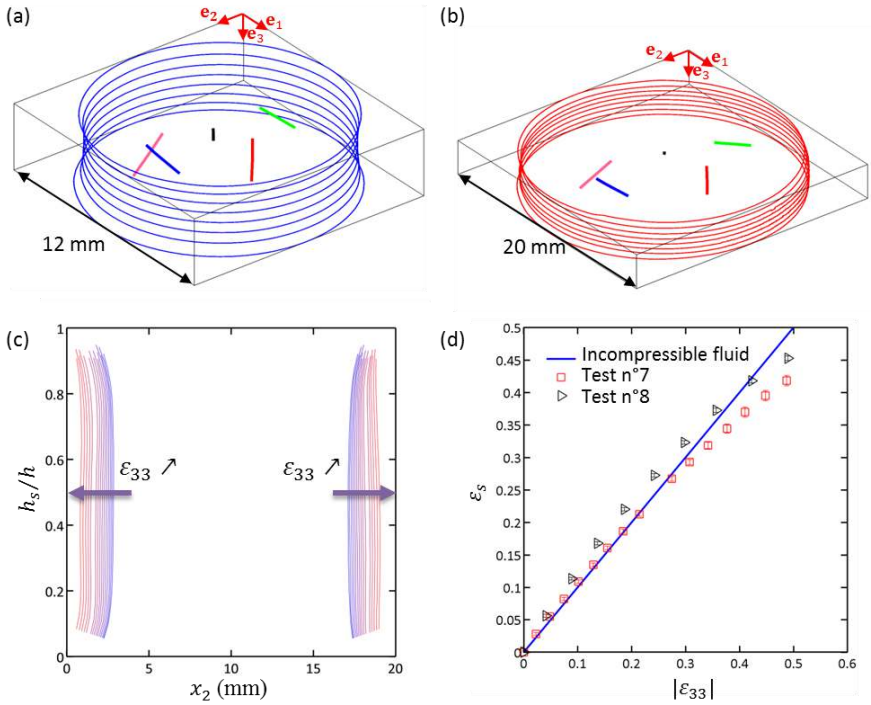

Fig. 3. (a) 3D view of the free surface and the fibre centrelines of a typical sample (sample 7) before (a) and after (b) a compression test. (c) 2D view in the $(\mathbf{e}_2, \mathbf{e}_3)$ *plane showing the evolution of the normalized profiles of the free surface of the same sample. (d) Evolutions of the surface strains* ε_s *with* $|\varepsilon_{33}|$ *for samples 7 and 8 during compression.*

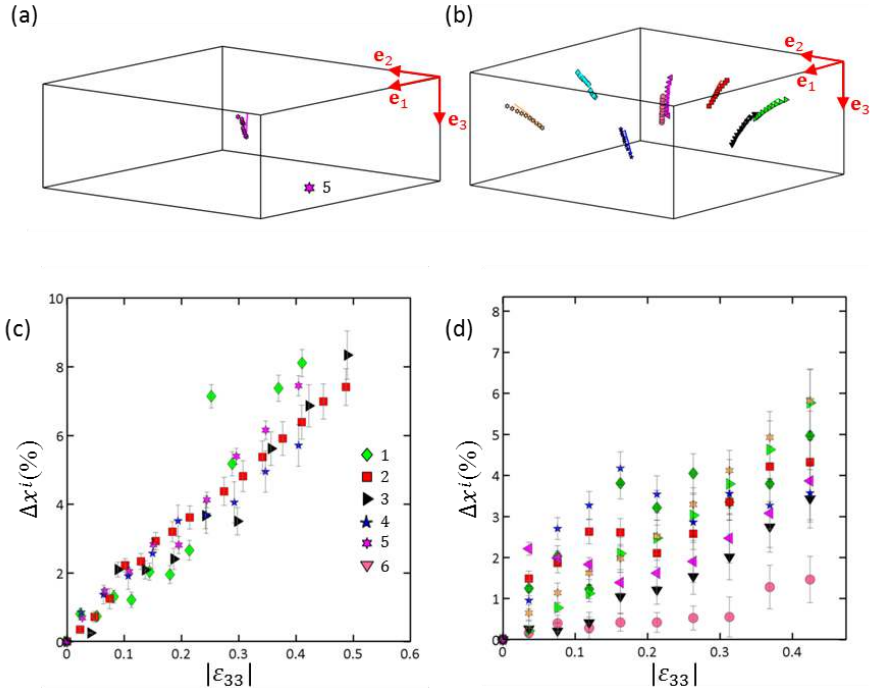

Fig. 4. Experimental (marks) and predicted (lines) trajectories of the fibrecentres of mass of fibres during compression of samples 1 (a) and 9 (b). Evolutions of the

deviations Δx^i as a function of the compression strain $|\varepsilon_{33}|$ for samples 1 to 6 containing one fibre (c) and for sample 9 containing eight fibres (d).

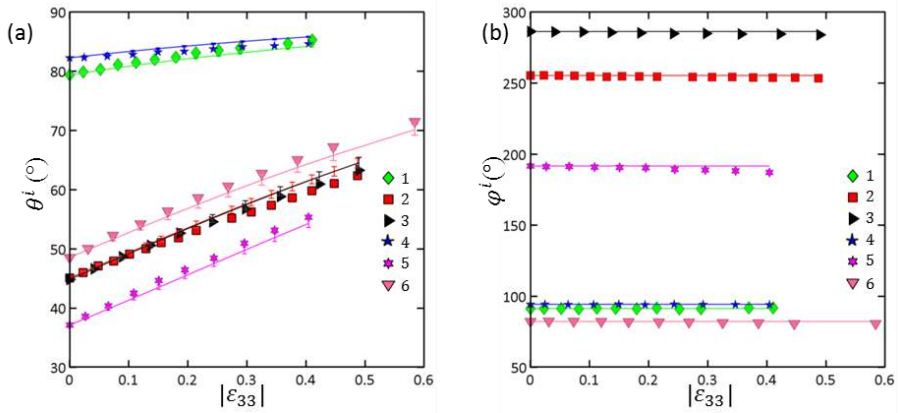

Fig. 5. Evolutions of the experimental (marks) and predicted (lines) angles θ^i (a) and φ^i (b) as a function of $|\varepsilon_{33}|$ for samples 1 to 6.

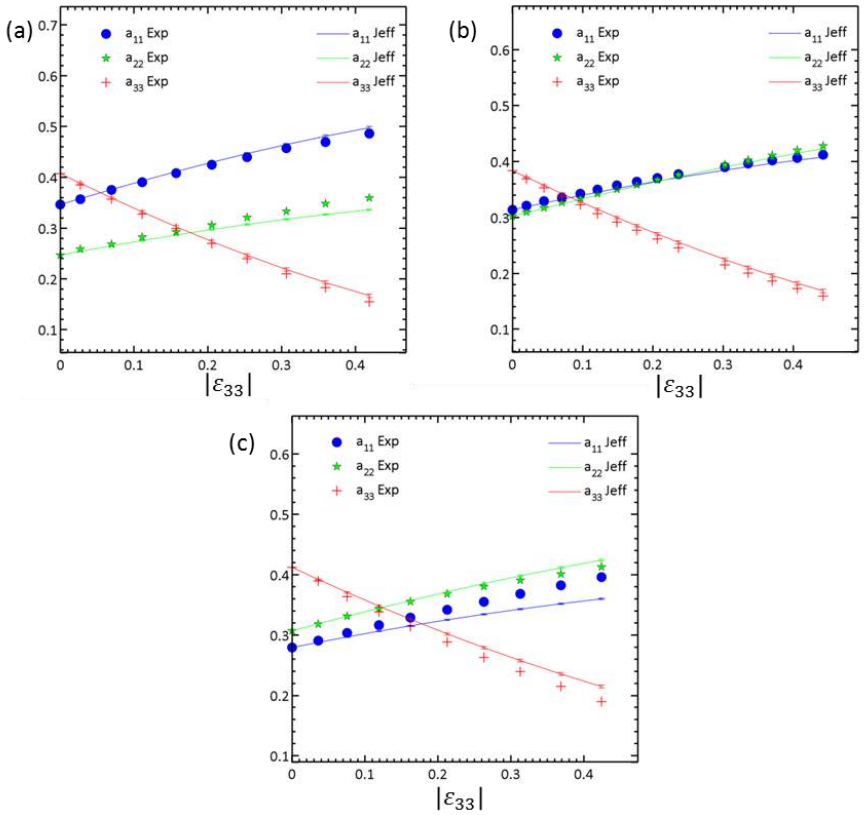

*Fig. 7. Experimental (marks) and predicted (lines) diagonal components a_{ii} of the second order fibre orientation tensor **A** as a function of $|\varepsilon_{33}|$ for samples 7 (a), 8 (b) and 9(c).*

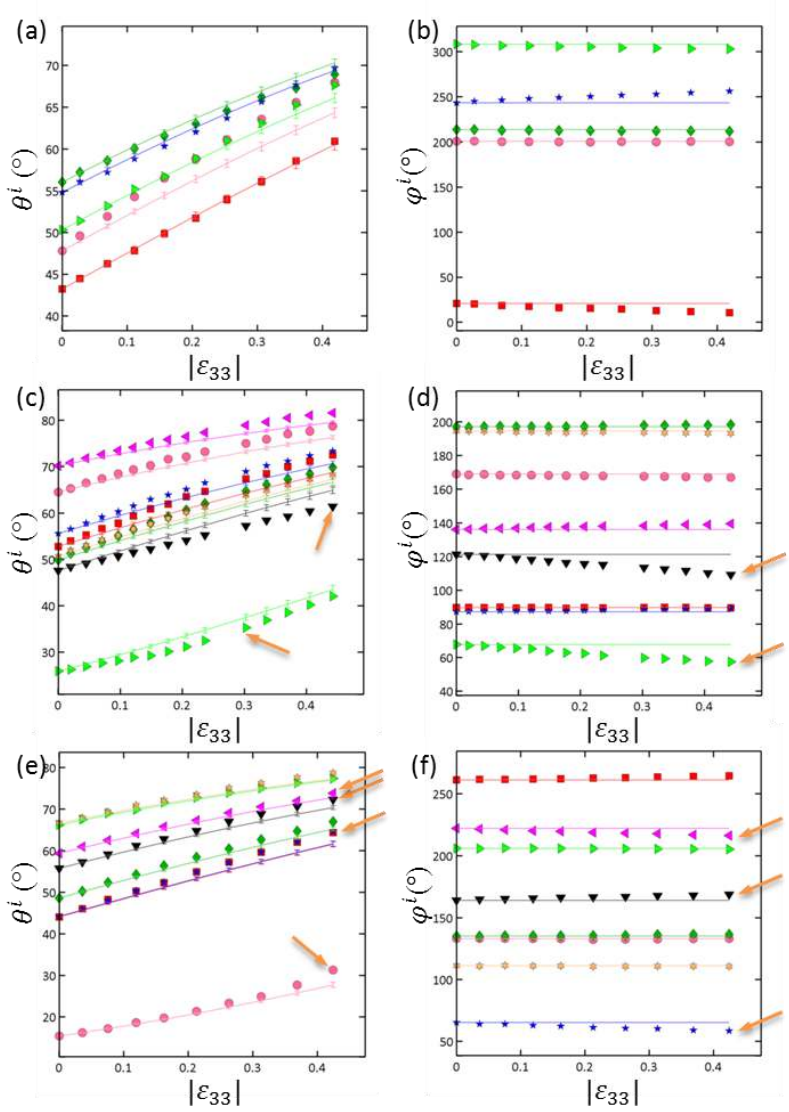

Fig. 6. Experimental (marks) and predicted (lines) evolutions of the fibre orientation angles θ^i(left) and φ^i(right) as a function of $|\varepsilon_{33}|$ for samples 7 (a-b), 8 (c-d) and 9(e-f). The orange arrows point to fibres that are close to one of the compression platens.